

A basic effect of cloud radiative effects on tropical sea-surface temperature

variability

Ying Li* and David W. J. Thompson

⁴ Department of Atmospheric Science, Colorado State University, Fort Collins, Colorado, USA

Dirk Olonscheck

Max Planck Institute for Meteorology, Hamburg, Germany

⁷ *Corresponding author address: Ying Li, Department of Atmospheric Science, Colorado State University, 3915 W. Laporte Ave. Fort Collins, CO 80521
⁸ E-mail: Ying.Li@colostate.edu

ABSTRACT

10 Cloud radiative effects (CREs) are known to play a central role in governing
11 the long-term mean distribution of sea-surface temperatures (SSTs). Very re-
12 cent work suggests that CREs may also play a role in governing the *variability*
13 of SSTs in the context of the El Niño/Southern Oscillation. Here, the authors
14 exploit numerical simulations in the Max Planck Institute Earth System Model
15 with two different representations of CREs to demonstrate that coupling be-
16 tween CREs and the atmospheric circulation has a much more general and
17 widespread effect on tropical climate than that indicated in previous work.

18 The results reveal that coupling between CREs and the atmospheric circu-
19 lation leads to robust increases in SST variability on timescales longer than
20 a month *throughout* the tropical oceans. Remarkably, cloud/circulation cou-
21 pling leads to more than a doubling of the amplitude of decadal-scale vari-
22 ability in tropical-mean SSTs. It is argued that the increases in tropical SST
23 variance derive primarily from the coupling between SSTs and shortwave
24 CREs: Coupling increases the memory in shortwave CREs on hourly and
25 daily timescales, and thus reddens the spectrum of shortwave CREs and in-
26 creases their variance on timescales spanning weeks to decades. Coupling
27 between SSTs and CREs does not noticeably affect the variance of SSTs in
28 the extratropics, where the effects from variability in CREs on the surface en-
29 ergy budget are much smaller than the effects from the turbulent heat fluxes.
30 The results indicate a basic but critical role of CREs in climate variability
31 throughout the tropics.

³² **1. Introduction**

³³ An increasing body of literature suggests that cloud radiative effects (CREs) play a key role
³⁴ in governing not only the *mean* atmospheric circulation and its response to global warming, but
³⁵ also its *variability* across a range of spatial and temporal scales. The advent of various remotely-
³⁶ sensed cloud products such as those derived from the CloudSAT /CALIPSO (Stephens et al. 2002)
³⁷ satellites has provided unprecedented insight into the vertical structure of clouds in the long-term
³⁸ mean (Zhang et al. 2007; Su et al. 2011; Su and Jiang 2013; Li et al. 2014b), and into the signatures
³⁹ of large-scale climate variability in various cloud properties in both the extratropics (Li et al.
⁴⁰ 2014a; Wall and Hartmann 2015; Li and Thompson 2016) and tropics (Eguchi and Shiotani 2004;
⁴¹ Masunaga et al. 2008; Chen and Genio 2009; Tromer and Rossow 2010; Jiang et al. 2011; Riley
⁴² et al. 2011; Ma and Kuang 2011; Yuan and Houze 2013; Crueger and Stevens 2015). Numerical
⁴³ experiments run with varying representations of CREs have revealed the central role of clouds in
⁴⁴ simulations of the mean tropospheric and stratospheric circulations (Fermepin and Bony 2014; Li
⁴⁵ et al. 2015, 2017; Harrop and Hartmann 2016; Watt-Meyer and Frierson 2017), in the simulated
⁴⁶ atmospheric circulation response to climate change (Ceppi et al. 2012, 2014; Ceppi and Hartmann
⁴⁷ 2015; Voigt and Shaw 2015, 2016; Ceppi and Hartmann 2016; Fläschner et al. 2018; Li et al.
⁴⁸ 2019; Voigt et al. 2019; Albern et al. 2019), and in the amplitude of climate variability in the
⁴⁹ context of the MJO (Lee et al. 2001; Crueger and Stevens 2015) and the spectrum of tropical
⁵⁰ waves (Zurovac-Jevtić et al. 2006; Lin et al. 2007).

⁵¹ Two recent studies have argued that cloud radiative feedbacks also play an important role in
⁵² governing the amplitude and periodicity of the El Niño/Southern Oscillation (ENSO) (Rädel et al.
⁵³ 2016; Middlemas et al. 2019). The studies both exploit “locked-clouds” experiments, but they
⁵⁴ were run on different numerical models and used slightly different experimental frameworks. In

both studies, the effects of CREs on the circulation are estimated by comparing output from 1) a control simulation where CREs are coupled to the atmospheric circulation and 2) a “locked-clouds” simulation where the cloud-related properties input into the model radiation code are decoupled from the atmospheric circulation. In the case of Middlemas et al. (2019), the CREs in the locked simulation were determined by repeating values of the CREs derived from a single sample year from the control simulation. As such, the CREs prescribed in the locked run have a similar diurnal and seasonal cycle to those found in the control run, but no interannual variability. In the case of Rädel et al. (2016), the CREs in the locked simulation were determined by randomizing the year assigned to each radiation call time step in the control output. The two studies yield slightly different results: Rädel et al. (2016) found that ENSO variability is enhanced across all timescales when CREs are coupled to the atmospheric circulation due to positive longwave cloud radiative feedbacks, whereas Middlemas et al. (2019) found ENSO variability is only enhanced on timescales shorter than 6 years, but reduced on timescales longer than that due to negative shortwave cloud radiative feedbacks.

One possible reason for the different responses in the two simulations is differences in the model treatment of shortwave and longwave feedbacks (Lloyd et al. 2011, 2012; Bellenger et al. 2014). For example, as discussed in Middlemas et al. (2019), the ENSO response to changes in cloud properties depends on the amplitudes in the CESM1.2 and MPI models of 1) the model shortwave and longwave cloud radiative feedbacks relative to 2) the other model feedbacks that are essential for the simulated ENSO variability.

Another possible reason is differences in the locking methodologies, in particular the effects of the locking methodologies on the auto-correlation of the prescribed cloud fields. The “locked-cloud” fields in Middlemas et al. (2019) consist of annually-repeating values drawn a single year from the control. The cloud fields in the control and locked simulations thus have roughly the

79 same autocorrelation. In contrast, the locked-cloud fields in Rädel et al. (2016) are randomized
80 such that they have no memory on timescales longer than two hours.

81 Here we hypothesize that removing the autocorrelation of the prescribed cloud fields in the
82 scrambling methodology is important for fully identifying the effects of cloud-circulation cou-
83 pling on the atmosphere. Specifically, we hypothesize that 1) cloud-circulation coupling imparts
84 memory to CREs that would not exist in the absence of forcing by the large-scale flow; 2) the
85 memory in CREs acts to increase the persistence of shortwave radiative fluxes at the surface; and
86 3) the reddening of the shortwave fluxes leads to increased low-frequency variance in the SST
87 field. It is suggested that a basic effect of coupling between clouds and the atmospheric circu-
88 lation is thus to redden the spectrum of shortwave CREs, hence reducing their variance on daily
89 and shorter timescales but increasing their variance on lower-frequency timescales. The increased
90 variance of shortwave CREs on low-frequency timescales, in turn, leads to notable increases in
91 the SST variance over the tropics, where surface temperature variability is dominated by the short-
92 wave radiative flux. Importantly, the coupling between CREs and the atmospheric circulation
93 enhances the month-to-month variability of SSTs by a factor of 2–3 not only in the tropical Pa-
94 cific, but *throughout* the tropical oceans. The coupling has little effect on SST variance over the
95 extratropics, where surface temperature variability is dominated by the turbulent heat fluxes.

96 **2. Locked-clouds simulations**

97 As in Rädel et al. (2016) and Middlemas et al. (2019), the influence of CREs on the circulation
98 are assessed by comparing output from 1) a control simulation where CREs are coupled to the
99 atmospheric circulation and 2) a “locked-clouds” simulation where the CREs are prescribed and
100 thus decoupled from the circulation.

101 The simulations were run on the latest version of the Max Planck Institute Earth System Model
102 at low resolution (MPI-ESM1.2-LR), and with preindustrial forcing (note that the experiments in
103 Rädel et al. (2016) were run on an earlier version of the model: the MPI-ESM1.0-LR). The model
104 has T63 (\sim 200 km) horizontal resolution and 47 vertical layers in the atmosphere component
105 (ECHAM6.3), and nominal 1.5° horizontal resolution and 40 vertical layers in the ocean com-
106 ponent (MPIOM 1.6.3). The MPI-ESM1.2-LR is the baseline version used in the sixth Coupled
107 Model Intercomparison Project (Eyring et al. 2016).

108 The locked simulations were performed in an analogous manner as described in Rädel et al.
109 (2016) and Olonscheck et al. (2019). That is:

- 110 1) Key cloud parameters - including cloud cover fraction and cloud liquid/ice water content at all
111 vertical levels - were saved from a 250-year long control simulation at every two-hour radiation
112 call (note that key cloud parameters are saved from just the first 50 years in Rädel et al. (2016)).
- 113 2) The cloud parameters from the control run were scrambled by randomizing the year assigned
114 to each time step, but not the hour or day. As such, the randomized cloud parameters have the
115 same long-term mean diurnal and seasonal cycles, have no memory from one time step to the
116 next (e.g., output at 00Z01Jan is assigned a different year than output at 02Z01Jan, etc), and
117 are decoupled from the circulation. As discussed below, the lack of autocorrelation in the cloud
118 fields plays an important role in changing the low-frequency variance of the attendant CREs.
- 119 3) The scrambled cloud fields were then read into the radiation code of the locked-clouds simula-
120 tion at every two-hour radiation call. The cloud locking method is only applied to the radiative
121 transfer scheme; all other model components use internally simulated clouds.

122 The control and locked-clouds simulations are both 250-yrs in length, but the first 50 years
123 of both simulations are discarded to account for the warming adjustment in the locked-clouds

¹²⁴ simulation as mentioned below. Note that a very similar scrambling methodology is also applied
¹²⁵ in Grise et al. (2019).

¹²⁶ Decoupling the cloud fields from the circulation leads to a weak warm bias in the locked-clouds
¹²⁷ simulations relative to the control run. A similar global-mean warming or cooling climate drift is
¹²⁸ found in other locked-clouds simulations, and is thought to arise from the small artificial radiative
¹²⁹ forcing that arises from the loss of spatio-temporal structure in clouds (Schneider et al. 1999;
¹³⁰ Langen et al. 2012; Mauritsen et al. 2013; Rädel et al. 2016; Middlemas et al. 2019; Olonscheck
¹³¹ et al. 2019). It is possible that the weak warm bias in the locked simulation could affect the
¹³² variance of temperature in the polar regions, since the variability in sea ice coverage depends
¹³³ on sea-ice thickness. For this reason, results are only shown equatorward of 70°S/N (readers are
¹³⁴ referred to Olonscheck et al. (2019) for a more detailed discussion on sea ice changes in analogous
¹³⁵ locking simulations). However, we view it unlikely that the small bias in mean temperature in the
¹³⁶ tropics will have a notable effect on the temperature variance there since 1) the differences in mean
¹³⁷ temperature between the control and locked simulation are roughly an order of magnitude smaller
¹³⁸ than 2) the typical differences in mean temperature between the coldest and warmest historical
¹³⁹ simulations in the CMIP5 archive (Mauritsen et al. 2012).

¹⁴⁰ **3. The influence of cloud radiative effects on tropical SST variability**

¹⁴¹ We focus our analysis on a comparison of month-to-month variability in 1) the control simula-
¹⁴² tion, where clouds are coupled to the circulation (hereafter referred to as the “interactive” clouds
¹⁴³ run) and 2) the “locked” clouds run, where clouds are decoupled from the circulation. The differ-
¹⁴⁴ ences in climate variability between the interactive and locked clouds simulations derive entirely
¹⁴⁵ from the role of coupling between CREs and the circulation.

146 Figure 1a shows the variance of monthly-mean SST anomalies in the interactive-clouds run.
147 The simulated SST variability is most pronounced in regions where 1) upwelling is important
148 (e.g., along the equator and near coastal regions) and 2) ocean heat transport and atmospheric
149 temperature advection are important (e.g., the western boundary current regions). Figure 1b shows
150 the same results for the locked-clouds run. At first glance, the patterns of SST variance in the
151 control interactive and locked clouds runs appear to differ only in the eastern tropical Pacific. But
152 closer inspection of the results reveals marked differences *throughout* the tropical oceans.

153 Figure 1c shows the ratios of the SST variances in the interactive and locked clouds simulations.
154 Values greater than one indicate regions where coupling between CREs and the circulation acts
155 to increase the variance in SSTs, and vice versa. Areas where the variance ratios are statistically
156 significant at the 95% significance level based on the F-statistic are stippled. The most prominent
157 ratios in Fig. 1c are found at tropical latitudes, particularly in the tropical Pacific. The increases in
158 variance over the tropical Pacific are consistent with the amplification of ENSO variability found
159 in Rädel et al. (2016). However, and importantly, similar increases in SST variance are found
160 throughout the tropical oceans, including variance ratios of 2–3 in the tropical Indian and Atlantic
161 ocean basins.

162 The differences in area-averaged SST variances between the interactive and locked clouds sim-
163 ulations are shown as a function of frequency in the power spectra in Fig. 2. The differences are
164 dramatic. Again, the differences in the power spectra over the Niño 3.4 region (Fig. 2a) are con-
165 sistent with the increases in ENSO variance noted in Rädel et al. (2016, cf. Fig. 2a) and the shift
166 to higher frequency ENSO variability found in Middlemas et al. (2019, cf. Fig. 4a). However,
167 the variances in the interactive simulation are increased substantially on interannual and decadal
168 time scale not only in the eastern tropical Pacific, but across the entire tropics (Figs. 2b-f). The
169 increases in variance in the tropical Indian (Fig. 2c), tropical western Pacific (Fig. 2d), and tropical

170 North and South Atlantic (Figs. 2e,f) oceans are most pronounced on timescales longer than \sim 5
171 years. Critically, the increases in tropical SST variance transcend the linear response to the model
172 ENSO (see Appendix B). That is, the increases in variances outside the eastern tropical Pacific
173 remain significant after the Niño 3.4 time series is linearly regressed from the output. As argued
174 in Section 4, the differences in monthly-mean SST variance shown in Fig. 1c and Fig. B1 arise
175 not from the projection of CREs onto ENSO per se, but rather from a more basic effect of CREs
176 on sea surface temperature.

177 The tropics-wide increases in SST variance are associated with a range of differences in various
178 other tropical fields. They are associated with increases in the variance of upper tropospheric
179 temperatures throughout the tropics (Fig. 3a), consistent with the facts that tropical atmospheric
180 temperatures are strongly modulated by the SST field and closely follow the moist adiabatic lapse
181 rate. Rädel et al. (2016) pose that such enhanced variance of atmospheric temperatures in the
182 interactive runs arises via longwave cloud radiative feedbacks. But as discussed in the next section,
183 we have a different interpretation of the source of increased variance.

184 The tropics-wide increases in SST variance are associated with increases in the variances of
185 convective precipitation (Fig. 3b), particularly over the tropical Pacific where the SST variance ra-
186 tios are largest. And they are associated with increases in the variances of the upper tropospheric
187 geopotential height field (Fig. 3c). The increases in the variance of upper tropospheric geopotential
188 height project onto the structure of the model equatorial planetary waves, as evidenced by the close
189 correspondence between 1) the equatorial troughs and ridges in the climatological-mean geopo-
190 tential height field (black contours in Fig. 3d) and 2) the variance ratios in the eddy geopotential
191 height field (shading in Fig. 3d).

192 **4. Interpretation**

193 Figures 1 and 2 reveal marked increases in SST variance throughout the tropics in simulations
194 run with interactive CREs. In this section, we explore the role of CRE in driving the tropical SST
195 variability in the context of surface energy budget rather than in the context of specific modes of
196 climate variability.

197 *a. Surface energy budget*

198 The energy budget for the surface mixed layer of the ocean can be expressed in monthly-mean
199 anomaly form as:

$$C_o \frac{\partial T'}{\partial t} = Q'_{SW} + Q'_{LW} + Q'_{LH} + Q'_{SH} + Q'_{EK} + Q'_{geo}, \quad (1)$$

200 where primes denote monthly-mean anomalies (departures from the long-term mean seasonal cy-
201 cle); T' is the anomalous temperature of the mixed layer (assumed proportional to the anomalous
202 SST); C_o is the effective heat capacity of the mixed layer ($C_o = C_p \rho h$, in which ρ and C_p are the
203 density and specific heat capacity at constant pressure of the seawater, i.e., $3850 \text{ J kg}^{-1} \text{K}^{-1}$), h is
204 the annual-mean mixed layer depth taken from the ocean model; and the Q' are the heatings due to
205 anomalous surface shortwave radiative flux (Q'_{SW}), longwave radiative flux (Q'_{LW}), latent heat flux
206 (Q'_{LH}), sensible heat flux (Q'_{SH}), advection by the Ekman flow (Q'_{EK}) and advection by the surface
207 geostrophic flow (Q'_{geo}). Here $Q_{EK} = -C_o \vec{V}_{EK} \cdot \nabla T$ and $Q_{geo} = -C_o \vec{V}_{geo} \cdot \nabla T$, in which \vec{V}_{EK} is
208 the Ekman flow induced by the wind stress (τ) and \vec{V}_{geo} is the geostrophic currents. We neglect
209 vertical advection and entrainment (Xie 1999) even though these processes are clearly important
210 along the coastal and equatorial upwelling zones.

211 Following Yu and Boer (2006), we can quantify the physical factors that drive the increases
212 in SST variance by diagnosing the attendant changes in the surface energy budget of Eq. (1).
213 Specifically, Eq. 1 can be manipulated to yield an expression for the temperature variance by a)

²¹⁴ taking the centered difference of Eq. 1, b) squaring the result, and c) taking the time-mean. As
²¹⁵ reviewed in Appendix A, the above operation yields the following expression for the temperature
²¹⁶ variance:

$$\sigma_T^2 = G \cdot \sigma_{\Sigma}^2 \cdot e \quad (2)$$

²¹⁷ where

- ²¹⁸ • σ_T^2 is the variance of the SST field.
- ²¹⁹ • $\sigma_{\Sigma}^2 = \sigma_{SW}^2 + \sigma_{LW}^2 + \sigma_{LH}^2 + \sigma_{SH}^2 + \sigma_{EK}^2 + \sigma_{geo}^2$ is the sum of the variances of the surface heat
²²⁰ fluxes and ocean heat transport. Larger variances in the flux and transport terms lead to larger
²²¹ variance in the SST field, and vice versa.

- ²²² • e includes the sum of the covariances between the heat flux terms (e.g., $e = 1 + \frac{2\Sigma(\text{cov}(Q_i, Q_j))}{\sigma_{\Sigma}^2}$),
²²³ where $\Sigma(\text{cov}(Q_i, Q_j)) = \text{cov}(Q'_{SW}, Q'_{LH}) + \text{cov}(Q'_{SW}, Q'_{SH}) + \text{cov}(Q'_{SW}, Q'_{EK}) + \dots$). e may be
²²⁴ viewed as an “efficiency factor” that measures the extent to which the variances in the flux and
²²⁵ transport terms operate independently in modifying the SST variance (Yu and Boer 2006).

- ²²⁶ • $G = \frac{2(\Delta t)^2}{C_o^2(1-r_2)}$ may be viewed as a “transfer factor” that accounts for the effects on the temper-
²²⁷ ature variance of the sampling timescale (Δt), the persistence (related to lag-2 autocorrelation
²²⁸ r_2), and the effective heat capacity (C_o) (Yu and Boer 2006).

²²⁹ The left and middle columns in Fig. 4 explore the contributions of the individual terms in σ_{Σ}^2 to
²³⁰ the variances in monthly-mean SSTs in the interactive and locked simulations. The right column
²³¹ shows the percent contributions of the individual variances in the left column to the total variances
²³² in the interactive run. The primary features in the figure are the following:

- ²³³ 1) The largest variances in the surface energy budget are found in association with the latent heat
²³⁴ fluxes and are located over the subtropical and midlatitude oceans (panels g and h).

- 235 2) The variances in the ocean heat transport peak over regions where the climatological-mean
236 SST gradients are largest (panels m and n) (Alexander 1992), and the variances in the sensible
237 heat fluxes peak over the western sides of the Northern Hemisphere ocean basins (panels j and
238 k), where there is commonly cold-advection in the atmosphere from the continents upstream
239 (Davis 1976; Miller 1992; Alexander 1992; Cayan 1992; Marshall et al. 2001; Alexander et al.
240 2002).
- 241 3) In the interactive simulation, the variances in the surface shortwave radiative fluxes have rel-
242 atively similar amplitude across the globe (panel a). As evidenced in panel c and discussed
243 further below, the shortwave radiative fluxes account for a comparatively large fraction of the
244 total variance in the energy budget over the tropics since the latent heat fluxes variance are
245 weakest there. The variances in the longwave radiative fluxes are relatively small and account
246 for a small fraction of the surface flux variance everywhere (panels d and f).
- 247 4) By far the most pronounced differences between the interactive and locked simulations are
248 found in the variances of the shortwave fluxes. The variances in monthly-mean shortwave
249 heat fluxes are $\sim 200 \text{ W}^2 \text{ m}^{-4}$ throughout much of the globe when clouds are coupled to the
250 circulation (panel a), but less than $\sim 20 \text{ W}^2 \text{ m}^{-4}$ in the locked simulation (panel b). As such
251 the shortwave variance ratios ($\frac{\sigma_{\text{SW, interactive}}^2}{\sigma_{\text{SW, locked}}^2}$) are as large as ~ 10 throughout much of the globe.
252 The surface radiative flux is derived from the all-sky radiative flux; the variances in clear-
253 sky radiative flux are of similar amplitude between the control and locked simulations. As
254 discussed below, such reduced variance of the monthly-mean all-sky shortwave radiative flux
255 in the locked simulation arises from the “whitening” of CREs when clouds are decoupled from
256 the circulation. That is, decoupling clouds from the circulation increases their variance on
257 sub-daily timescales, but decreases their variance on weekly and longer timescales.

258 From Eq. 2, it follows that the ratios of temperature variance between the interactive and locked
 259 run can be diagnosed as:

$$\frac{\sigma_T^2}_{\text{interactive}} = \frac{\sigma_\Sigma^2}_{\text{interactive}} \cdot \frac{e_{\text{interactive}}}{e_{\text{locked}}} \cdot \frac{G_{\text{interactive}}}{G_{\text{locked}}} \quad (3)$$

260 Based on the results shown in Fig. 4, we assume 1) the variances associated with the shortwave
 261 and longwave radiative flux in the locked-clouds run are very small (Figs. 4b,e), 2) the variances
 262 associated other terms in the surface energy budget in the locked-clouds runs are approximately
 263 equal to those in the interactive run (compare Figs. 4g,h; Figs. 4j,k; Figs. 4m,n) and 3) the percent-
 264 age contributions from the longwave radiative flux to the total variance can be neglected (Fig. 4f).

265 Based on the above, the first term in the RHS of Eq. 3 can be written as:

$$\frac{\sigma_\Sigma^2}_{\text{interactive}} \approx \frac{\sigma_\Sigma^2}_{\text{interactive}}}{(\sigma_{LH}^2 + \sigma_{SH}^2 + \sigma_{EK}^2 + \sigma_{geo}^2)_{\text{interactive}}} \approx \frac{1}{1 - (\frac{\sigma_{SW}^2}{\sigma_\Sigma^2})_{\text{interactive}}}. \quad (4)$$

266 The simple scaling in Eq. 4 suggests that 1) the changes in the total variance of the surface energy
 267 flux between the interactive and locked-clouds simulations (LHS of Eq. 4) should peak over re-
 268 gions where 2) the shortwave cloud flux variance makes the largest contribution to the total energy
 269 flux variance in the interactive simulation (i.e., as shown in Fig. 4c).

270 Figure 5 quantifies the contributions of the various ratios in Eqs. 3–4 to the changes in temper-
 271 ature variance between the interactive and locked simulations. Figure 5a reproduces the ratios of
 272 the temperature variances from Fig. 1c (i.e., it shows the LHS of Eq. 3). Figure 5b shows the prod-
 273 uct of the ratios between the interactive and locked simulations of 1) the surface flux and transport
 274 variances, 2) the “efficiency” factors (e), and 3) “transfer” factors (G) (i.e., it shows the RHS of
 275 Eq. 3). Figure 5c shows the first factor only from the RHS of Eq. 3, which is equivalent to the
 276 sum of the results in the left column in Fig. 4 ($\sigma_\Sigma^2_{\text{interactive}}$) divided by the sum of the results in the
 277 middle column ($\sigma_\Sigma^2_{\text{locked}}$). Figures 5c, d show the results of the scaling approximation from Eq. 4,
 278 and highlight the role of the shortwave radiative fluxes.

Comparing the results in Figs. 5a–c, it is clear that the ratios of SST variances between the interactive and locked simulations (Fig. 5a) can be qualitatively reproduced by the decomposition given in Eq. 3 (Fig. 5b). The decomposition, in turn, is dominated by the first factor on the RHS of Eq. 3. That is, the increases in SST variance in the interactive simulation arise primarily from the increases in the variance of the surface energy fluxes (Fig. 5c). The other two factors on the RHS of Eq. 3 (i.e., the “efficiency” and “transfer” factors) are dominated by 1) decreases in the covariances between the radiative fluxes in the locked run and 2) weak increases in SST persistence in the tropical and extratropical oceans in the interactive run (Fig. C1). However, they play a relatively small role in the amplification of tropical SST variance between the interactive and locked simulations, as evidenced by the similarities between Figs. 5b and 5c. The fact that the differences in SST variance between the interactive and locked simulations peak at tropical latitudes (Fig. 5a) is consistent with the fact that the shortwave radiative fluxes play a more prominent role in the total variance of the surface energy fluxes at tropical latitudes than they do at extratropical latitudes (Figs. 4c and 5d; Eq. 4).

The key results in Figs. 4 and 5 are thus:

- 1) the preponderance of the differences in monthly-mean SST variance between the interactive and locked simulations (Fig. 1c) arise from the attendant differences in the monthly-mean shortwave radiative flux variances (Figs. 4a and 4b), and
- 2) the differences in monthly-mean SST variance peak in the tropics (Fig. 1c) since the variance in the shortwave radiative fluxes accounts for a relatively large fraction of the total variances in the surface energy budget there (Figs. 4c and 5d).

300 b. Relationships between the hour-to-hour persistence and month-to-month variance of cloud frac-
301 tion

302 Why does the variance of the monthly-mean shortwave radiative flux increase when clouds are
303 coupled to the atmospheric circulation? To understand this, we first consider the power spectrum
304 of two standardized, random time series: 1) a white noise time series and 2) a red-noise time
305 series with lag-one autocorrelation of $r_1 = 0.9$. For the purpose of comparison to the numerical
306 model output, the increment between time steps is defined as two-hours. By construction, both
307 time series have the same variance: one. However, the white noise time series has larger variance
308 than the red noise time series at periods shorter than ~ 28 hours (i.e., 14 time steps), whereas the
309 red noise time series has much larger variance than the white noise time series at all periods longer
310 than ~ 28 hours (Fig. 6a). The cutoff period at which a standardized red noise time series exhibits
311 larger variance than a standardized white noise time series ranges from ~ 14 time steps (i.e., 28
312 hours in the case of data sampled every 2 hours) when $r_1 = 0.9$ to about ~ 5 time steps (i.e., 10
313 hours) when $r_1 = 0.1$ (see dashed lines in Fig. 6a).

314 Now consider the time series of total cloud fraction at a sample tropical grid point from the
315 control interactive model simulations sampled at two-hourly intervals (corresponding to radiation
316 call). In the interactive simulation, the cloud fraction has memory from one radiation call (every
317 two hours) to the next of roughly $r_1 \approx 0.9$. However, in the locked simulation - by construction -
318 the cloud fraction has no memory from two-hour period to the next ($r_1 = 0$). The total variance of
319 the cloud fraction time series is identical in both the interactive and locked simulations. However,
320 as is the case for the idealized white and red noise time series, the differences in the variance of
321 cloud fraction between the two simulations are a function of frequency. The variance of cloud
322 fraction in the interactive simulation is less than the variance of cloud fraction in the locked sim-

ulation at periods less than \sim 24 hours, but exceeds the variance of cloud fraction in the locked simulation at periods greater than \sim 1 day (Fig. 6b).

Hence, the increases in the variances of cloud fraction - and thus in the variances in shortwave CREs (Figs. 4a) and SSTs (Fig. 5) – in the interactive simulations arise from the reddening of the cloud field when it is coupled to the atmospheric circulation. *A basic effect of two-way coupling between clouds and the atmospheric circulation in the simulation is thus to increase the variance of CREs on timescales longer than a few days at the expense of shorter timescales.* As noted earlier, the increased variances in shortwave CREs have largest effect on the variance in SSTs at tropical latitudes, where the shortwave radiative fluxes account for a large fraction of the total variance in the surface energy fluxes. They have only a weak effect on the variances in SSTs at extratropical latitudes, where the shortwave radiative fluxes play a small role in the total variance in the surface energy fluxes.

5. Concluding remarks

It is long established that CREs play a central role in determining Earth's mean climate. It is becoming increasingly clear that they also play a key role in Earth's climate variability across a range of timescales. In two recent studies, Rädel et al. (2016) and Middlemas et al. (2019) argue that the inclusion of coupling between the atmospheric circulation and clouds projects onto the variance of the ENSO, primarily due to the projection of longwave or shortwave CREs onto ENSO physics. Here we argue that coupling between the atmospheric circulation and CREs leads to a much broader and more basic effect on the climate system: Cloud circulation coupling leads to increases in the variance of SSTs on timescales from months to decades that are apparent throughout the tropical oceans (Figs. 1c and 2) and can not be explained as the linear response to simulated ENSO variability (Appendix B).

346 We hypothesize that the increases in tropical SST variance in the interactive simulation arise
347 from the “reddening” of shortwave CREs when clouds are coupled to the circulation. Coupling
348 between the atmospheric circulation and clouds increases the memory in clouds on subdaily and
349 day-to-day timescales (e.g., the e-folding timescale of cloud fraction is \sim 1–2 days in sample time
350 series drawn from the interactive simulation; Fig. 6). The reddening of the cloud field due to the
351 memory inherent in the large-scale atmospheric circulation leads to a reduction in the variance
352 of cloud fraction on timescales less than a few days, but large increases in the variance of cloud
353 fraction on timescales greater than a few days (Fig. 6). Decomposition of the surface energy budget
354 (Figs. 4 and 5) reveals that it is the resulting increases in the variance of monthly-mean shortwave
355 CREs that lead to the increases in SST variance when clouds are coupled to the circulation. The
356 increases in SST variance are most clear in the tropics, where the shortwave heat fluxes account
357 for the largest fraction of the total variance in the surface energy budget (Figs. 4c and 5d). They
358 are less clear in the extratropics, where SST variability is dominated by the surface turbulent heat
359 fluxes (Fig. 4i).

360 The hypothesis accounts for enhanced SST variability on timescales spanning months to decades
361 throughout the tropical oceans when clouds are coupled to the atmospheric circulation. A key as-
362 sumption in the hypothesis is that cloud-circulation coupling does not change the total variance in
363 clouds and CREs (i.e., by construction the total variance is held fixed in the locked and interactive-
364 cloud simulations). Rather cloud-circulation coupling is theorized to impart memory to - and thus
365 enhance the low-frequency variance of - clouds and their radiative effects. Such memory would
366 not exist in the absence of the coupling of clouds to large-scale dynamics.

367 The results shown here support our hypothesis that the reddening of shortwave CREs by
368 cloud/circulation feedbacks leads to a reddening of SST variability. It is difficult to quantita-
369 tively compare our results with those published in Middlemas et al. (2019) without reproducing

their simulations in the climate model used here. Hence, it is unclear whether the differences in results between our study and that study arises from differences in a) the locking methodologies or b) the cloud-radiative feedbacks and cloud-circulation coupling schemes used in the different climate models. It would be interesting to further test our hypothesis by running additional simulations on the MPI climate model in which the cloud fields are a) decoupled from the circulation but b) retain the same autocorrelation. It would also be interesting to explore and test the robustness of our hypothesis in climate models with different representations of CREs and in geographic regions corresponding to different convective regimes (i.e., cloud-circulation coupling is a function of convective regime; Bony and Dufresne 2005). We plan to test our hypothesis in more detail in a companion study.

The results shown here reveal the remarkable effect that cloud-circulation coupling has on the amplitude of SST variability on intraseasonal, interannual and even decadal time scales (Figs. 1c and 2). Hence a key implication of our hypothesis is that the amplitude of SST variability in numerical simulations depends critically on model renditions of CREs and cloud-circulation coupling. This is important, since tropical SSTs provide a source of potential predictability for the climate system across a range of timescales, and are linked to a host of surface climate impacts throughout the tropics and extratropics. The implications of our hypothesis for climate impacts and predictability are being explored for a companion study.

Acknowledgment. We thank Thorsten Mauritsen for assistance with the numerical model output. We gratefully acknowledge three anonymous reviewers whose insightful comments led to significant improvements to the manuscript. We also thank Eleanor A. Middlemas and Kevin M. Grise for providing comments and suggestions. Y.L. is funded by NSF Climate and Large-Scale Dynamics (AGS-1547003) and NASA JPL (1439268). D.W.J.T. is funded by NSF Climate

393 and Large-Scale Dynamics (AGS-1343080 and AGS-1547003). D.O. is funded by the Max Planck
 394 Society (MPG). We thank the German Climate Computing Centre (DKRZ) for providing extensive
 395 computational resources.

396 APPENDIX A

397 **Decomposition of the factors that contribute to the variance in SST**

398 The variance of SST is derived from the surface energy equation (Eq. 1), and follows Yu and Boer
 399 (2006). Taking the centered difference of Eq. 1:

$$400 C_o \frac{T'(t + \Delta t) - T'(t - \Delta t)}{2\Delta t} = Q'_{SW} + Q'_{LW} + Q'_{LH} + Q'_{SH} + Q'_{EK} + Q'_{geo}, \quad (A1)$$

400 where Δt is 1 month.

401 Taking the square of Eq. A1 and the time average (denoted by overbar), the *lhs* of the resulting
 402 equation is approximately equal to

$$\begin{aligned} &\approx \frac{C_o^2}{2(\Delta t)^2} \left(\overline{T(t)'^2} - \overline{T'(t + \Delta t)T'(t - \Delta t)} \right) \\ &= \frac{C_o^2(1 - r_2)}{2(\Delta t)^2} \sigma_T^2 \end{aligned} \quad (A2)$$

403 where σ_T^2 is the variance of the monthly-mean SST anomaly, and r_2 is lag-2 autocorrelation of
 404 SST anomaly computed as $\frac{\overline{T'(t + \Delta t)T'(t - \Delta t)}}{\overline{T(t)'^2}}$.

405 The *rhs* of the square and time average of Eq. A1 is equal to:

$$\sigma_\Sigma^2 + 2\Sigma(cov(Q_i, Q_j)), \quad (A3)$$

406 where σ_Σ^2 is the total variances of the six heat fluxes and transport related variances: $\sigma_\Sigma^2 = \sigma_{SW}^2 +$
 407 $\sigma_{LW}^2 + \sigma_{LH}^2 + \sigma_{SH}^2 + \sigma_{EK}^2 + \sigma_{geo}^2$; and $\Sigma(cov(Q_i, Q_j))$ is the summed covariances of the individual
 408 six components: $\Sigma(cov(Q'_i, Q'_j)) = cov(Q'_{SH}, Q'_{LH}) + cov(Q'_{SH}, Q'_{SW}) + cov(Q'_{SH}, Q'_{EK}) + \dots$. Note

⁴⁰⁹ that the variances and covariances terms involving the radiation fluxes are approximately zero in
⁴¹⁰ the locked-clouds simulation (e.g., Figs. 4b, e).

⁴¹¹ Thus the variance of the SST can be approximately estimated from Eqs. A2–A3 as:

$$\sigma_T^2 = \frac{2(\Delta t)^2}{C_o^2(1-r_2)}(\sigma_{\Sigma}^2 + 2\Sigma(\text{cov}(Q_i, Q_j))) \quad (\text{A4})$$

$$= G \cdot \sigma_{\Sigma}^2 \cdot e \quad (\text{A5})$$

⁴¹² where $G = \frac{2(\Delta t)^2}{C_o^2(1-r_2)}$, $e = 1 + \frac{2\Sigma(\text{cov}(Q_i, Q_j))}{\sigma_{\Sigma}^2}$.

APPENDIX B

The robustness of the changes in SST variance to changes in ENSO variability

⁴¹³ Figures 1c and 2 reveal that coupled CREs leads to increases in SST variance not only in the
⁴¹⁴ tropical central/eastern Pacific, but also in the tropical western Pacific, tropical Indian and Atlantic
⁴¹⁵ oceans. Figure B1 tests whether the changes in SST variance outside the central/eastern tropical
⁴¹⁶ Pacific can be explained as linear response to SST anomalies in the ENSO region. The figure is
⁴¹⁷ identical to Figure 1, except that the Niño3.4 index has been linearly regressed from the SST data
⁴¹⁸ at every grid point. The regression is based on contemporaneous values of the SST field and the
⁴¹⁹ ENSO index, but similar results are derived after lagging the SST field by three months and with
⁴²⁰ other ENSO indices (not shown). By construction, the regression does not account for non-linear
⁴²¹ relationships between ENSO variability and the SST field. As illustrated in Fig. B1, the increases
⁴²² in SST variances outside the eastern tropical Pacific are not linearly related to changes in SST
⁴²³ variability in the ENSO region, and thus appear to occur independently of the model ENSO.

APPENDIX C

The contributions of “efficiency factor” e and “transfer factor” G

428 Figure 5c shows the first term on the *rhs* of Eq. 3 (i.e., the ratios of the surface flux and transport
429 variances). Here in Fig. C1 we show the contributions of the second and third terms in the *rhs* of
430 Eq. 3. Panel (a) shows the ratios of the “efficiency factors” - which arise mainly from differences
431 in the sum of the covariances between the heat flux terms. Panel (b) shows the ratios of the
432 “transfer factors”- which arise from differences in SST persistence as calculated from the lag-2
433 auto-correlation. The ratios in the “efficiency factors” are generally less than 1, indicating the
434 covariance terms are generally smaller in the interactive-cloud simulation than they are in the
435 locked-cloud simulation. The ratios of the “transfer factors” are generally positive since SST
436 persistence is slightly longer in the interactive simulation. Overall, the changes in the two factors
437 are relatively weak relative to the changes in the variances of the surface energy fluxes (Fig. 5c).

438 References

- 439 Albern, N., A. Voigt, and J. G. Pinto, 2019: Cloud-radiative impact on the regional responses of
440 the midlatitude jet streams and storm tracks to global warming. *J. Adv. Model. Earth Syst.*, **11**,
441 1940–1958.
- 442 Alexander, M. A., 1992: Midlatitude atmosphere-ocean interaction during El Niño. Part I: The
443 North Pacific Ocean. *J. Climate*, **5**, 944–958.
- 444 Alexander, M. A., I. Bladé, M. Newman, J. R. Lanzante, N.-C. Lau, and J. D. Scott, 2002: The
445 atmospheric bridge: Influence of ENSO teleconnections on air-sea interaction over the global
446 oceans. *J. Climate*, **15**, 2205–2231.
- 447 Bellenger, H., E. Guilyardi, J. Leloup, M. Lengaigne, and J. Vialard, 2014: ENSO repre-
448 sentation in climate models: from CMIP3 to CMIP5. *Clim. Dynam.*, **42**, 1999–2018, doi:
449 10.1007/s00382-013-1783-z.

- 450 Bony, S., and J.-L. Dufresne, 2005: Marine boundary layer clouds at the heart of tropi-
451 cal cloud feedback uncertainties in climate models. *Geophys. Res. Lett.*, **33**, L17810, doi:
452 10.1029/2005GL023851.
- 453 Cayan, D. R., 1992: Latent and sensible heat flux anomalies over the northern oceans: driving the
454 sea temperature. *J. Phys. Oceanogr.*, **22**, 859–881.
- 455 Ceppi, P., and D. L. Hartmann, 2015: Connections between clouds, radiation, and midlatitude
456 dynamics: a review. *Curr. Clim. Change Rep.*, doi:10.1007/s4061-015-0010-x.
- 457 Ceppi, P., and D. L. Hartmann, 2016: Clouds and the atmospheric circulation response to warming.
458 *J. Climate*, **29**, 783–799, doi:10.1002/2014GL060043.
- 459 Ceppi, P., Y.-T. Hwang, D. M. W. Frierson, and D. L. Hartmann, 2012: Southern Hemisphere jet
460 latitude biases in CMIP5 models linked to shortwave cloud forcing. *Geophys. Res. Lett.*, **39**,
461 L19708, doi:10.1029/2012GL053115.
- 462 Ceppi, P., M. D. Zelinka, and D. L. Hartmann, 2014: The response of the Southern Hemispheric
463 eddy-driven jet to future changes in shortwave radiation in CMIP5. *Geophys. Res. Lett.*, **41**,
464 3244–3250, doi:10.1002/2014GL060043.
- 465 Chen, Y., and A. D. D. Genio, 2009: Evaluation of tropical cloud regimes in observations and a
466 general circulation mode. *Clim. Dynam.*, **32**, 355–369, doi:10.1007/S00382-008-0386-6.
- 467 Crueger, T., and B. Stevens, 2015: The effect of atmospheric radiative heating by clouds on the
468 Madden-Julian Oscillation. *J. Adv. Model. Earth Syst.*, doi:10.1002/2015MS000434.
- 469 Davis, R. E., 1976: Predictability of sea surface temperature and sea level pressure anomalies over
470 the North Pacific Ocean. *J. Phys. Oceanogr.*, **6**, 249–266.

- 471 Eguchi, N., and M. Shiotani, 2004: Intraseasonal variations of water vapor and cirrus clouds in the
472 tropical upper troposphere. *J. Geophys. Res.*, **109**, D12 106, doi:10.1029/2003JD004314.
- 473 Eyring, V., S. Bony, G. A. Meehl, C. A. Senior, B. Stevens, R. J. Stouffer, and K. E. Taylor, 2016:
474 Overview of the Coupled Model Intercomparison Project Phase 6 (CMIP6). *Geosci. Model Dev.*,
475 **9**, 1937–1958, doi:10.5194/gmd-9-1937-2016.
- 476 Fermepin, S., and S. Bony, 2014: Influence of low-cloud radiative effects on tropical circulation
477 and precipitation. *J. Adv. Model. Earth Syst.*, **06**, doi:10.1002/2013MS000288.
- 478 Fläschner, D., T. Mauritsen, B. Stevens, and S. Bony, 2018: The signature of shallow circulations,
479 not cloud radiative effects, in the spatial distribution of tropical precipitation. *J. Climate*, 9489–
480 9505, doi:10.1175/JCLI-D-18-0230.1.
- 481 Grise, K. M., B. Medeiros, J. J. Benedict, and J. G. Olson, 2019: Investigating the influence of
482 cloud radiative effects on the extratropical storm tracks. *Geophys. Res. Lett.*, **46**, 7700–7707.
- 483 Harrop, B. E., and D. L. Hartmann, 2016: The role of cloud radiative heating in determining
484 the location of the ITCZ in aquaplanet simulations. *J. Climate*, **29**, 2741–2763, doi:10.1175/
485 JCLI-D-15-0521.1.
- 486 Jiang, X., D. E. Waliser, J.-L. Li, and C. Woods, 2011: Vertical structures of cloud water associated
487 with the boreal summer intraseasonal oscillation based on CloudSat observations and ERA-
488 Interim reanalysis. *Clim. Dynam.*, **10**, doi:10.1007/s00382-010-0853-8.
- 489 Langen, P. L., R. G. Graversen, and T. Mauritsen, 2012: Separation of contributions from radiative
490 feedbacks to polar amplification on an aquaplanet. *J. Climate*, **25**, 3010–3024, doi:10.1175/
491 JCLI-D-11-00246.1.

- 492 Lee, M.-I., I.-S. Kang, J.-K. Kim, and B. E. Mapes, 2001: Influence of cloud-radiation interaction
493 on simulating tropical intraseasonal oscillation with an atmospheric general circulation model.
494 *J. Geophys. Res.*, **106**, 14 219–14 233, doi:10.1029/2001JD900143.
- 495 Li, Y., and D. W. J. Thompson, 2016: Observed signatures of the barotropic and baroclinic annular
496 modes in cloud vertical structure and cloud radiative effects. *J. Climate*, **29**, 4723–4740.
- 497 Li, Y., D. W. J. Thompson, and S. Bony, 2015: The influence of atmospheric cloud ra-
498 diative effects on the large-scale atmospheric circulation. *J. Climate*, **28**, 7263–7278, doi:
499 10.1175/JCLI-D-14-00825.1.
- 500 Li, Y., D. W. J. Thompson, S. Bony, and T. M. Merlis, 2019: Thermodynamic control on the
501 poleward shift of the extratropical jet in climate change simulations. *J. Climate*, **32**, 917–934.
- 502 Li, Y., D. W. J. Thompson, and Y. Huang, 2017: The influence of atmospheric cloud radiative
503 effects on the large-scale stratospheric circulation. *J. Climate*, **30**, 5621–5635, doi:10.1175/
504 JCLI-D-16-0643.1.
- 505 Li, Y., D. W. J. Thompson, Y. Huang, and M. Zhang, 2014a: Observed linkages between the
506 Northern Annular Mode/North Atlantic Oscillation, cloud incidence, and cloud radiative forc-
507 ing. *Geophys. Res. Lett.*, **41**, 1681–1688, doi:10.1002/2013GL059113.
- 508 Li, Y., D. W. J. Thompson, G. L. Stephens, and S. Bony, 2014b: A global survey of the linkages
509 between cloud vertical structure and large-scale climate. *J. Geophys. Res.*, **119**, 3770–3792,
510 doi:10.1002/2013JD020669.
- 511 Lin, J.-L., D. Kim, M. Lee, and I. Kang, 2007: Effects of cloud-radiative heating on atmospheric
512 general circulation model (AGCM) simulations of convectively coupled equatorial waves. *J.*
513 *Geophys. Res.*, **112**, D24 107, doi:10.1029/2006JD008291.

- 514 Lloyd, J., E. Guilyardi, and H. Weller, 2011: The role of atmosphere feedbacks during ENSO in
515 the CMIP3 models. Part II: using AMIP runs to understand the heat flux feedback mechanisms.
516 *Clim. Dynam.*, **37**, 1271–1292, doi:10.1007/s00382-010-0895-y.
- 517 Lloyd, J., E. Guilyardi, and H. Weller, 2012: The role of atmosphere feedbacks during ENSO
518 in the CMIP3 Models. Part III: The shortwave flux feedback. *J. Climate*, **25**, 4275–4293, doi:
519 10.1175/JCLI-D-11-00178.1.
- 520 Ma, D., and Z. Kuang, 2011: Modulation of radiative heating by the Madden-Julian Oscilla-
521 tion and convectively coupled Kelvin Waves as observed by CloudSat. *Geophys. Res. Lett.*, **38**,
522 L21 813.
- 523 Marshall, J., H. Johnson, and J. Goodman, 2001: A study of the interaction of the North Atlantic
524 Oscillation with ocean circulation. *J. Climate*, **14**, 1399–1421.
- 525 Masunaga, H., M. Satoh, and H. Miura, 2008: A joint satellite and global cloud-resolving
526 model analysis of a Madden-Julian Oscillation event: Model diagnosis. *J. Geophys. Res.*, **113**,
527 D17 210, doi:10.1029/2008JD009986.
- 528 Mauritsen, T., R. G. Graversen, D. Klocke, P. L. Langen, B. Stevens, and L. Tomassini,
529 2013: Climate feedback efficiency and synergy. *Clim. Dynam.*, **41**, 2539–2554, doi:10.1007/
530 s00382-013-1808-7.
- 531 Mauritsen, T., and Coauthors, 2012: Tuning the climate of a global model. *J. Adv. Model. Earth
532 Syst.*, **4**, M00A01, doi:10.1029/2012MS000154.
- 533 Middlemas, E. A., A. C. Clement, B. Medeiros, and B. Kirtman, 2019: Cloud radiative feedbacks
534 and El Niño Southern Oscillation. *J. Climate*, **32**, 4661–4680, doi:10.1175/jcli-d-18-0842.1.

- 535 Miller, A. J., 1992: Large-scale ocean-atmosphere interactions in a simplified coupled model of
536 the midlatitude wintertime circulation. *J. Atmos. Sci.*, **49**, 273–286.
- 537 Olonscheck, D., T. Mauritsen, and D. Notz, 2019: Arctic sea-ice variability is primarily
538 driven by atmospheric temperature fluctuations. *Nature Geosci.*, **12**, 430–434, doi:10.1038/
539 s41561-019-0363-1.
- 540 Rädel, G., T. Mauritsen, B. Stevens, D. Dommelget, D. Dommelget, D. Matei, K. Bellomo,
541 and A. Clement, 2016: Amplification of El Niño by cloud longwave coupling to atmospheric
542 circulation. *Nature Geoscience*. *Nature Geosci.*, **9**, 106–110.
- 543 Riley, E. M., B. E. Mapes, and S. N. Tulich, 2011: Clouds Associated with the Madden–Julian
544 Oscillation: A New Perspective from CloudSat. *J. Atmos. Sci.*, **68**, 3032–3051, doi:10.1175/
545 JAS-D-11-030.1.
- 546 Schneider, E. K., B. P. Kirtman, and R. S. Lindzen, 1999: Tropospheric water vapor and climate
547 sensitivity. *J. Atmos. Sci.*, **56**, 1649–1658.
- 548 Stephens, G., and Coauthors, 2002: The CloudSat mission and the A-train: A new dimension of
549 space-based observations of clouds and precipitation. *Bull. Amer. Meteor. Soc.*, **83**, 1771–1790,
550 doi:10.1175/BAMS-83-12-1771.
- 551 Su, H., and J. H. Jiang, 2013: Tropical clouds and circulation changes during the 2006–07 and
552 2009–10 El Niños. *J. Climate*, **26**, 399–413, doi:10.1175/JCLI-D-12-00152.1.
- 553 Su, H., J. H. Jiang, J. Teixeira, A. Gettelman, X. Huang, G. Stephens, D. Vane, and V. S. Perun,
554 2011: Comparison of regime-sorted tropical cloud profiles observed by CloudSat with GEOS5
555 analyses and two general circulation model simulations. *J. Geophys. Res.*, **116**, D09104, doi:
556 10.1029/2010JD014971.

- 557 Tromeur, E., and W. B. Rossow, 2010: Interaction of tropical deep convection with the large-scale
558 circulation in the MJO. *J. Climate*, **23**, 1837–1853, doi:10.1175/2009JCLI3240.1.
- 559 Voigt, A., N. Albern, and G. Papavasileiou, 2019: The atmospheric pathway of the cloud-radiative
560 impact on the circulation response to global warming: Important and uncertain. *J. Climate*, **32**,
561 3051–3067, doi:10.1175/JCLI-D-18-0810.1.
- 562 Voigt, A., and T. A. Shaw, 2015: Radiative changes of clouds and water vapor shape circulation
563 response to global warming. *Nature Geosci.*, **8**, 102–106, doi:10.1038/ngeo2345.
- 564 Voigt, A., and T. A. Shaw, 2016: Impact of regional atmospheric cloud radiative changes on shifts
565 of the extratropical jet stream in response to global warming. *J. Climate*, **29**, 8399–8421, doi:
566 10.1175/JCLI-D-16-0140.1.
- 567 Wall, C. J., and D. L. Hartmann, 2015: On the influence of poleward jet shift on Shortwave cloud
568 feedback in GCMs. *J. Adv. Model. Earth Syst.*, **07**, doi:10.1002/2015MS000520.
- 569 Watt-Meyer, O., and D. M. W. Frierson, 2017: Local and remote impacts of atmospheric cloud
570 radiative effects onto the eddy-driven jet. *Geophys. Res. Lett.*, **44**, 10 036–10 044, doi:10.1002/
571 2017GL074901.
- 572 Xie, S.-P., 1999: A dynamic ocean-atmosphere model of the tropical Atlantic decadal variability.
573 *J. Climate*, **12**, 64–70.
- 574 Yu, B., and G. J. Boer, 2006: The variance of sea surface temperature and projected changes with
575 global warming. *Clim. Dynam.*, **26**, 801–821, doi:10.1007/s00382-006-0117-9.
- 576 Yuan, J., and R. A. Houze, 2013: Deep convective systems observed by A-Train in the trop-
577 ical Indo-Pacific region affected by the MJO. *J. Atmos. Sci.*, **70**, 456–486, doi:10.1175/
578 JAS-D-12-057.1.

- 579 Zhang, Y., S. Klein, G. G. Mace, and J. Boyl, 2007: Cluster analysis of tropical clouds using
CloudSat data. *Geophys. Res. Lett.*, **34**, L12 813, doi:10.1029/2007GL029336.
- 580 581 Zurovac-Jevtić, D., S. Bony, and K. Emanuel, 2006: On the role of clouds and moisture in tropical
waves: A two-dimensional model study. *J. Atmos. Sci.*, **63**, 2140–2154.

583 LIST OF FIGURES

- Fig. 1.** The effect of interactive clouds on SST variance. (a) Variances of monthly-mean SST anomalies from the 200-yr interactive-clouds run. (b) Variances of monthly-mean SST anomalies from the 200-yr locked-clouds run. (c) Ratio of the variances between the interactive and locked runs. Ratios >1 indicate larger variability in the interactive run, and vice versa. Stippling indicates regions where the ratios are significant at the 95% level. The black boxes in (c) are the regions used for calculating the power spectra of the area averaged SST anomalies in Fig. 2.

Fig. 2. Power spectra of SST anomaly time series for indicated regions. Power spectra of SST anomaly time series averaged over (a) Niño 3.4, (b) entire tropics (15°S – 15°N), (c) tropical Indian ocean (10°S – 10°N , 50° – 100°E), (d) tropical western Pacific (10°S – 10°N , 100°E – 180°), (e) tropical north Atlantic (0° – 15°N , 315° – 340°E), and (f) tropical south Atlantic (15°S – 0° , 20°W – 10°E). Results for the interactive-clouds simulation are indicated by the blue lines, and for the locked-clouds simulation are indicated by the red lines. Regions are indicated by the black boxes in Fig. 1c.

Fig. 3. The effects of interactive clouds on tropical climate. Ratio of the variances between the interactive and locked runs of (a) atmospheric temperature at 300 hPa, (b) convective precipitation, (c) geopotential height at 150 hPa, and (d) eddy geopotential height at 150 hPa. The black contours superimposed on panel d denote the long-term mean geopotential height at 150 hPa (contour interval: 14000, 14100, 14110, 14120, 14130 m...). Results in shading are based on monthly-mean anomalies.

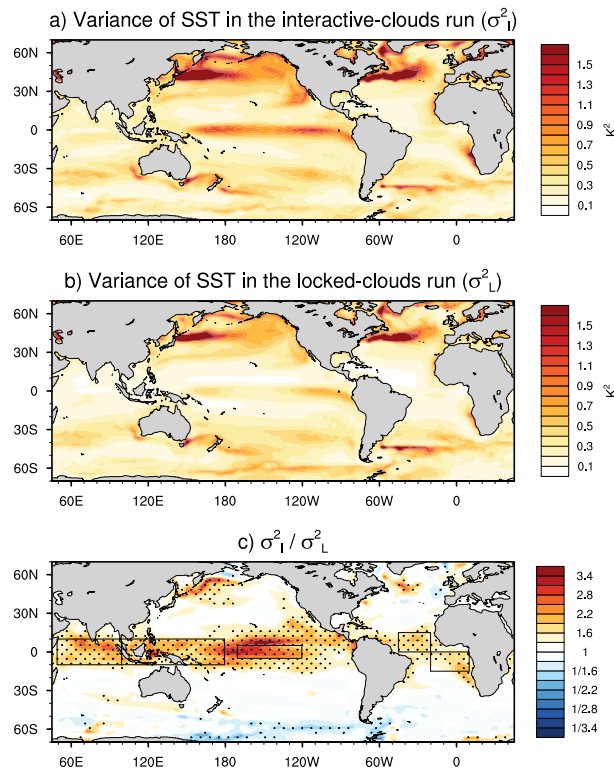
Fig. 4. Variances in the surface energy fluxes. (a, b) surface shortwave radiative flux, (d, e) long-wave radiative flux, (g, h) latent heat flux, (j, k) sensible heat flux, (m, n) heat advection by the meridional Ekman and geostrophic current. Results for (left column) the 200-yr interactive-clouds simulation and (middle column) the 200-yr locked-clouds simulation. The right column is the percentage contribution of each term to the total variance in the interactive-clouds simulation. Results are based on monthly-mean anomalies.

Fig. 5. Identifying the physical factors responsible for the increases in SST variance. (a) The ratios of the surface temperature variance between the interactive and locked simulations (reproduced from Fig. 1c). (b) The product of all three terms on the *rhs* of Eq. 3. (c) The contribution of the ratios in the sums of the surface fluxes (the first factor on the *rhs* of Eq. 3). (d) The results of the approximation in Eq. 4, which highlights the dominant role of the SW radiative fluxes in the ratios shown in panel c (see text for details). Results are based on monthly-mean anomalies.

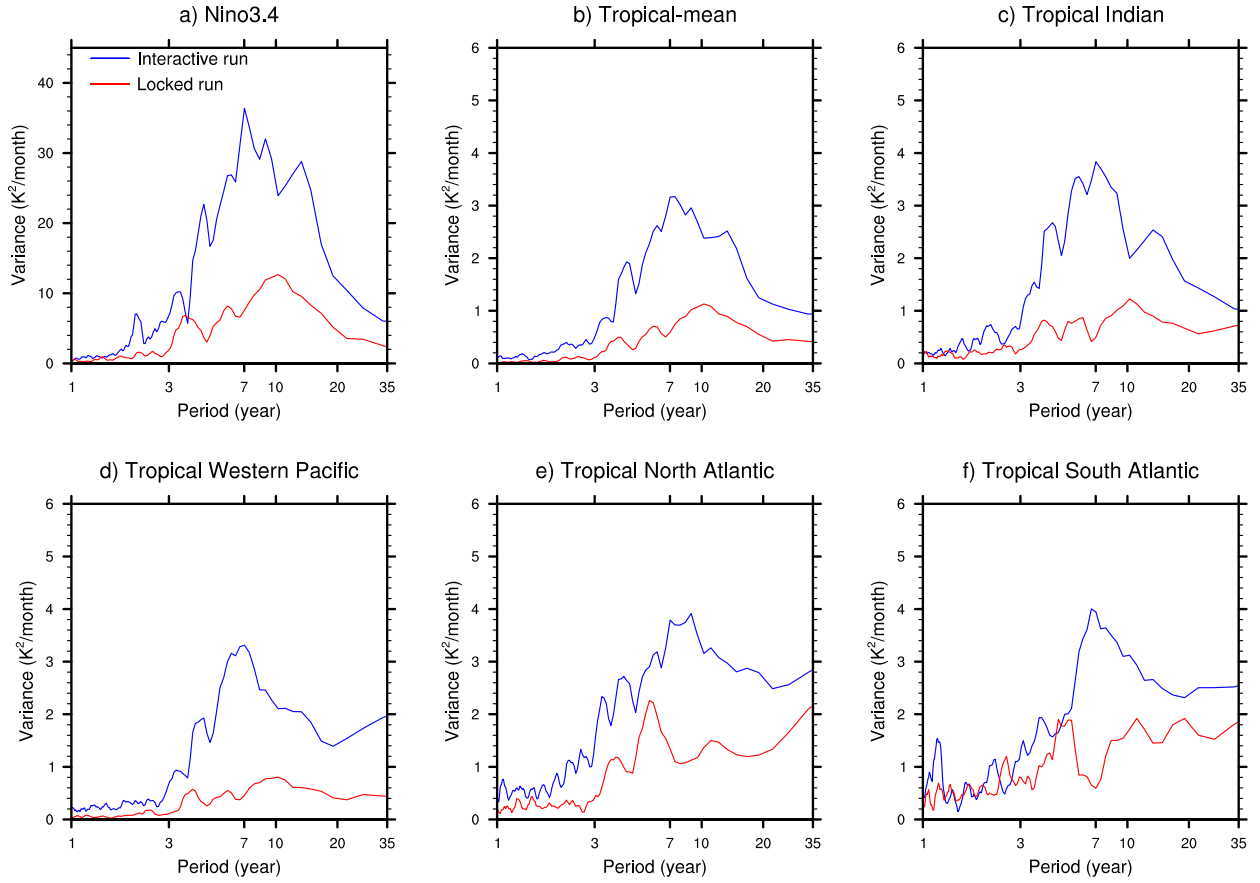
Fig. 6. The importance of persistence in the variance of cloud fraction. (a) Power spectra for a randomly generated red noise time series with lag-one autocorrelation of $r_1 = 0.9, 0.5$, and 0.1 (dashed lines) and a white noise time series with $r_1 = 0$ (solid line). (b) Power spectra for time series of cloud fraction at a sample tropical grid point ($0^{\circ}, 180^{\circ}$) used in the interactive-clouds run (dashed line) and the locked-clouds run (solid). The cloud fraction time series are 50-yr long and sampled at two-hourly intervals. The randomly generated time series used to construct the top panel are the same length and same time step interval as the cloud fraction time series.

Fig. B1. SST variances in the interactive and locked simulation after linearly removing the effects of ENSO from the data. Same as Fig. 1, but for results after subtracting linearly regressing the Niño 3.4 index (SSTs averaged over 5°N – 5°S , 170°W – 120°W as indicated by black box in panel c) from the SST data at all grid points.

Fig. C1. As in Fig. 5c, but for (a) the ratios of the “efficiency” factors (the second term on the *rhs* of Eq. 3), and (b) the ratio of the “transfer” factors (the third term on the *rhs* of Eq. 3). 37



631 FIG. 1. The effect of interactive clouds on SST variance. (a) Variances of monthly-mean SST anomalies from
 632 the 200-yr interactive-clouds run. (b) Variances of monthly-mean SST anomalies from the 200-yr locked-clouds
 633 run. (c) Ratio of the variances between the interactive and locked runs. Ratios >1 indicate larger variability in
 634 the interactive run, and vice versa. Stippling indicates regions where the ratios are significant at the 95% level.
 635 The black boxes in (c) are the regions used for calculating the power spectra of the area averaged SST anomalies
 636 in Fig. 2.



637 FIG. 2. Power spectra of SST anomaly time series for indicated regions. Power spectra of SST anomaly
 638 time series averaged over (a) Niño 3.4, (b) entire tropics (15°S – 15°N), (c) tropical Indian ocean (10°S – 10°N ,
 639 50° – 100°E), (d) tropical western Pacific (10°S – 10°N , 100°E – 180°), (e) tropical north Atlantic (0° – 15°N , 315° –
 640 340°E), and (f) tropical south Atlantic (15°S – 0° , 20°W – 10°E). Results for the interactive-clouds simulation are
 641 indicated by the blue lines, and for the locked-clouds simulation are indicated by the red lines. Regions are
 642 indicated by the black boxes in Fig. 1c.

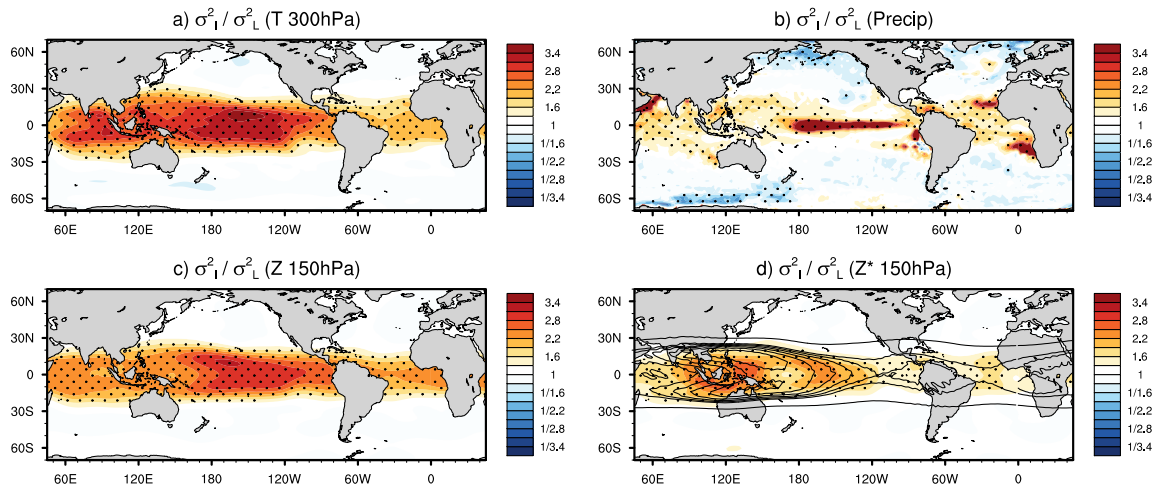


FIG. 3. The effects of interactive clouds on tropical climate. Ratio of the variances between the interactive and locked runs of (a) atmospheric temperature at 300 hPa, (b) convective precipitation, (c) geopotential height at 150 hPa, and (d) eddy geopotential height at 150 hPa. The black contours superimposed on panel d denote the long-term mean geopotential height at 150 hPa (contour interval: 14000, 14100, 14110, 14120, 14130 m...). Results in shading are based on monthly-mean anomalies.

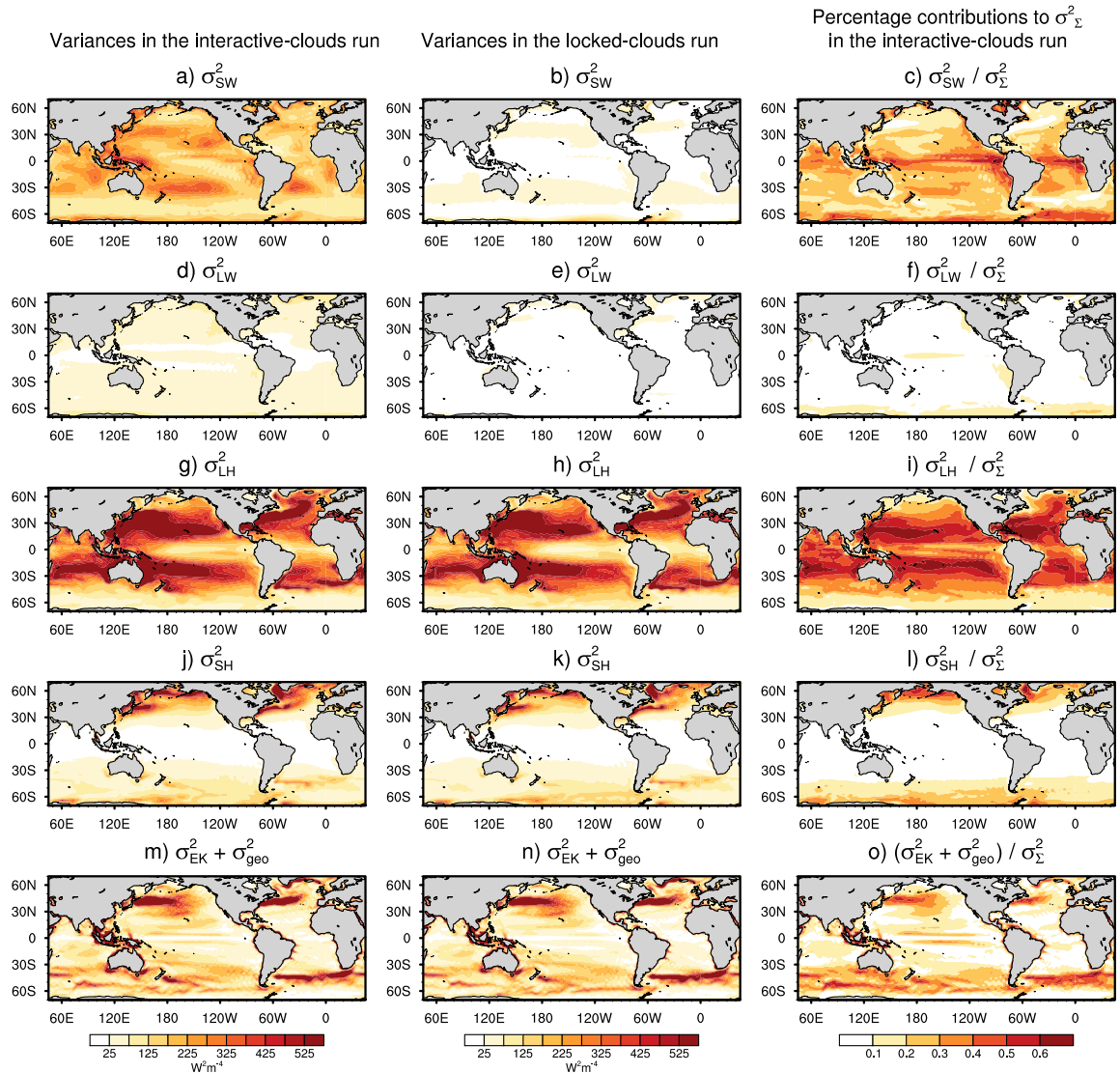


FIG. 4. Variances in the surface energy fluxes. (a, b) surface shortwave radiative flux, (d, e) longwave radiative flux, (g, h) latent heat flux, (j, k) sensible heat flux, (m, n) heat advection by the meridional Ekman and geostrophic current. Results for (left column) the 200-yr interactive-clouds simulation and (middle column) the 200-yr locked-clouds simulation. The right column is the percentage contribution of each term to the total variance in the interactive-clouds simulation. Results are based on monthly-mean anomalies.

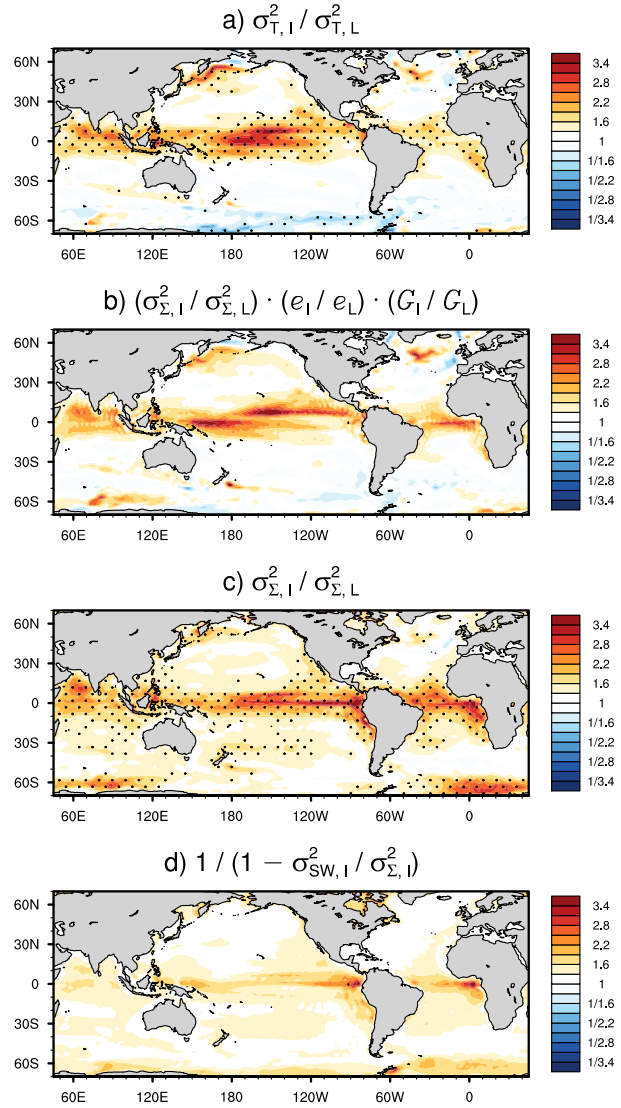
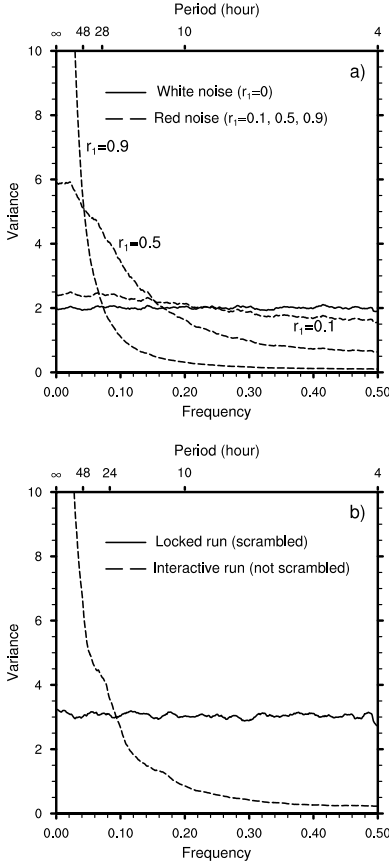
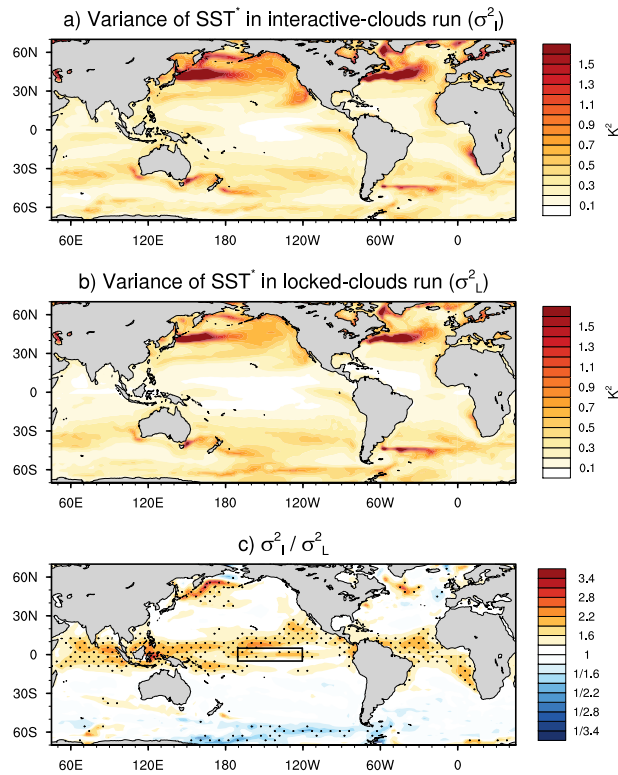


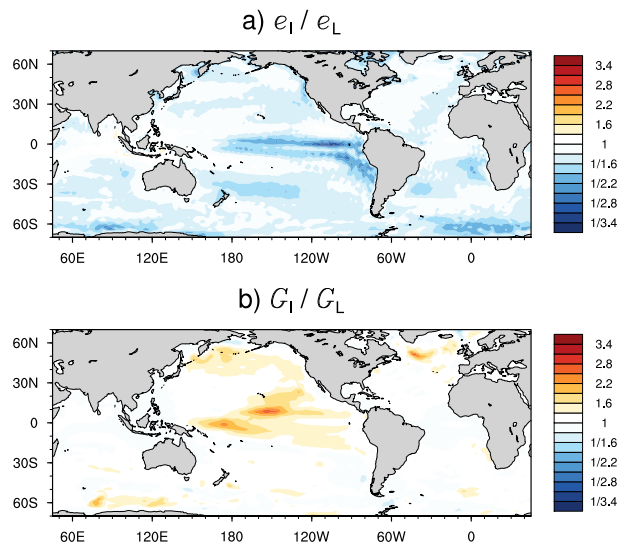
FIG. 5. Identifying the physical factors responsible for the increases in SST variance. (a) The ratios of the surface temperature variance between the interactive and locked simulations (reproduced from Fig. 1c). (b) The product of all three terms on the *rhs* of Eq. 3. (c) The contribution of the ratios in the sums of the surface fluxes (the first factor on the *rhs* of Eq. 3). (d) The results of the approximation in Eq. 4, which highlights the dominant role of the SW radiative fluxes in the ratios shown in panel c (see text for details). Results are based on monthly-mean anomalies.



659 FIG. 6. The importance of persistence in the variance of cloud fraction. (a) Power spectra for a randomly
 660 generated red noise time series with lag-one autocorrelation of $r_1 = 0.9, 0.5$, and 0.1 (dashed lines) and a white
 661 noise time series with $r_1 = 0$ (solid line). (b) Power spectra for time series of cloud fraction at a sample tropical
 662 grid point ($0^\circ, 180^\circ$) used in the interactive-clouds run (dashed line) and the locked-clouds run (solid). The cloud
 663 fraction time series are 50-yr long and sampled at two-hourly intervals. The randomly generated time series used
 664 to construct the top panel are the same length and same time step interval as the cloud fraction time series.



665 Fig. B1. SST variances in the interactive and locked simulation after linearly removing the effects of ENSO
 666 from the data. Same as Fig. 1, but for results after subtracting linearly regressing the Niño 3.4 index (SSTs
 667 averaged over 5°N–5°S, 170°W–120°W as indicated by black box in panel c) from the SST data at all grid
 668 points.



669 Fig. C1. As in Fig. 5c, but for (a) the ratios of the “efficiency” factors (the second term on the *rhs* of Eq. 3),
 670 and (b) the ratio of the “transfer” factors (the third term on the *rhs* of Eq. 3).